mathematics

Article

Reconstruction of Unsteady Wind Field Based on CFD and Reduced-Order Model

Guangchao Zhang * and Shi Liu

School of Energy Power and Mechanical Engineering, North China Electric Power University, Beijing 102206, China; liushi@ncepu.edu.cn
* Correspondence: ZGC15966651591@163.com

Abstract: Short-term wind power forecasting is crucial for updating the wind power trading strategy, equipment protection and control regulation. To solve the difficulty surrounding the instability of the statistical model and the time-consuming nature of the physical model in short-term wind power forecasting, two innovative wind field reconstruction methods combining CFD and a reduced-order model were developed. In this study, POD and Tucker decomposition were employed to obtain the spatial–temporal information correlation of 2D and 3D wind fields, and their inverse processes were combined with sparse sensing to reconstruct multi-dimensional unsteady wind fields. Simulation and detailed discussion were performed to verify the practicability of the proposed algorithms. The simulation results indicate that the wind speed distributions could be reconstructed with reasonably high accuracy (where the absolute velocity relative error was less than 0.8%) using 20 sensors (which only accounted for 0.04% of the total data in the 3D wind field) based on the proposed algorithms. The factors influencing the results of reconstruction were systematically analyzed, including all-time steps, the number of basis vectors and 4-mode dimensions, the diversity of CFD databases, and the reconstruction time. The results indicated that the reconstruction time could be shortened to the time interval of data acquisition to synchronize data acquisition with wind field reconstruction, which is of great significance in the reconstruction of unsteady wind fields. Although there are still many studies to be carried out to achieve short-term predictions, both unsteady reconstruction methods proposed in this paper enable a new direction for short-term wind field prediction.

Keywords: proper orthogonal decomposition; tucker decomposition; wind field reconstruction; spatial-temporal information correlation; computational fluid dynamics; reduced-order model

MSC: 15A18; 15A23; 15A29; 15A72

Citation: Zhang, G.; Liu, S. Reconstruction of Unsteady Wind Field Based on CFD and Reduced-Order Model. *Mathematics* **2023**, *11*, 2223. https://doi.org/10.3390/math11102223

Academic Editors: Sergey Ershkov and Evgeniy Yur'evich Prosviryakov

Received: 15 April 2023
Revised: 6 May 2023
Accepted: 7 May 2023
Published: 9 May 2023

1. Introduction

Wind energy, as the protagonist of energy transformation in response to energy shortages and the environmental pollution crisis, has attracted worldwide attention for its development and utilization. Nowadays, with the increasing installed capacity of wind power, the development of wind power still faces the serious phenomenon of wind abandonment and power limitation [1]. Despite the tremendous advantages of grid-connected wind power, due to the uncertainty and intermittent nature of wind power, its ever-increasing installed capacity poses tremendous challenges to the power system [2]. Improving the accuracy of wind speed and power prediction is one of the most important means of solving the above problems. Accurate power prediction is a prerequisite for the accurate grid-connected dispatch of wind power. It can not only help power dispatchers make accurate and effective decisions to reduce the adverse impact of wind power on the entire power grid but also greatly reduce the cost of wind power, bringing enormous economic benefits to the power market [3].

Many research methods on high reliability and efficiency have been introduced in the related research of wind forecasting, which can be divided into the mathematical statistics

method [4–8], the physical model method [9–13] and other methods [14–18] according to the model principle.

Mathematical statistical prediction methods usually use historical data to build statistical models and infer future values by observing the relationships among data. Contrary to physical forecasting methods, mathematical methods require a great deal of historical data to train statistical models. The traditional statistical method commonly uses a large amount of historical data to model through the steps of pattern recognition, parameter estimation and model tests to determine a mathematical model containing a time series and then derive the prediction model [19]. For example, Miyoshi et al. [20] combined simulation with real-world sensor data using statistical mathematics and the dynamic system theory to achieve wind speed prediction using numerical weather prediction (NWP). However, due to the difficulty of setting and estimating parameters of high-order mathematical models, traditional statistical methods are often used as reference models with the improvement of prediction accuracy [21]. With the development of computer science and data processing technology, the artificial network prediction (ANN) algorithm has been developed and is very effective at predicting wind speed, which has strong self-learning, self-organization and adaptive ability [22]. Madhiarasan et al. [23] employed hidden neuron estimation in a multi-layer perceptron network to predict wind speed. The developed neural network model has a compact structure, which can improve forecasting accuracy and accelerate the convergence rate. The accuracy of the mathematical prediction method depends heavily on the number of sample data, which results in a large amount of data calculation in the early stage. If the dimension of the prediction parameters is high, the calculation speed of the mathematical prediction is greatly reduced. Another obvious defect is that the mathematical statistical model generally fails to accurately predict extreme weather conditions that are not included in the historical database, which can lead to wind farms failing to respond in time when complex or special weather conditions occur [24].

As the most primitive and reliable prediction method, physical statistical forecasting is usually based on Numerical Weather Prediction (NWP), which uses basic physical principles such as the law of mass conservation, momentum conservation and energy conservation to forecast wind speed [25]. In recent years, related commercial companies have developed many models based on numerical weather prediction which have been widely used in commercial projects [26–28]. The Global Forecasting System (GFS) developed by the U.S. Environmental Monitoring Center has the widest application range. It mainly uses a series of meteorological data (including temperature, pressure, distribution of obstacles or surface roughness, etc.) to achieve global forecasting by solving complex mathematical models [27]. With the development of computer science, CFD has been widely adopted as an important tool in various fields, such as physics and medicine, making an indelible contribution to promoting scientific development and improving human healthcare [29,30]. Most physical models are based on CFD to simulate atmospheric flow. In the real wind field, solving hydrodynamic equations and obtaining wind speed distribution with high spatial resolution requires much calculation time. Although the reliability of the results can be guaranteed, high accuracy also results in long calculation times and high requirements for computer performance, so it is not suitable for application in wind speed prediction scenarios that require a fast response [31].

Considering the defects of both models, the technical route of PT (Process Tomography) can be introduced into wind field reconstruction. Wind field reconstruction can be regarded as the application of PT technology in the field of wind resource utilization, i.e., only a small amount of real-time measurement data can be applied to realize the overall reproducibility of physical information, such as the wind direction and wind speed, by solving inverse problems. The inverse problem is usually solved by using sparse measurement data to obtain a large amount of original data. If the characteristics of the original data can be obtained before the calculation starts, the accuracy and efficiency of reconstruction will be greatly improved. The application of reconstruction in the field of short-term wind prediction addresses the uncertainty of statistical methods and large computational loads

of physical methods, but the application of reduced models is urgently needed. With the development of the theory of computational mathematics, the research on reduced-order models has been quite in-depth. POD and Tucker decomposition, with their convenience and high precision, have become the most mature means of order reduction in many models and have been widely used in the field of matrix and tensor [32]. For example, Jiang et al. [33] employed POD to combine sparse sensor observations with the CFD database to quickly estimate the airflow field. Qin et al. [34] employed singular value decomposition (SVD) and principal component analysis (PCA) to reduce the dimensions of the wind speed database and combined sparse sensor measurements to achieve high-precision wind field reconstruction. Zhang et al. [35] proposed a sensor and CFD database fusion technology based on Tucker decomposition, which achieved the purpose of obtaining a 3D wind field from sparse measurements.

Although these approaches have been extensively studied in different fields, they are all based on steady-state physical fields. Significantly, the steady-state condition is unreasonable in real wind farms, especially for completely unknown incoming flows. In addition, in previous studies, the systematic comparison and analysis of POD and Tucker decomposition in 2D and 3D wind field reconstructions have not been enough, especially when analyzing the reconstruction efficiency and impact of the CFD database on reconstruction results.

Motivated by the above problems, the main research goals of the present paper contain two parts: First, we verified the reliability of POD and Tucker decomposition in a multi-dimensional unsteady wind field reconstruction. Second, we explored the factors affecting reconstruction errors to optimize the reconstruction results of multi-dimensional unsteady wind fields.

To achieve these research goals, an unsteady environment is created by changing wind speed inlet conditions, and the POD and Tucker decomposition can be employed for 2D and 3D unsteady wind field reconstructions, respectively. In addition, based on the given wind field environment, the factors influencing the results of reconstruction can be systematically analyzed. Through simulation and detailed discussion, both methods enabled the accurate and fast reconstruction of multi-dimensional unsteady wind fields, providing a new direction in which the instability of statistical models and the time-consuming physical model can be solved.

The chief originality of this study can be summarized as follows: Firstly, the combination of offline CFD simulation and reduced-order model can greatly save calculation time while ensuring the accuracy of reconstruction, which creatively combine wind field reconstruction with short-term wind forecasting, addressing the uncertainty of statistical methods and large computational loads of physical methods. Secondly, different from the previous studies on steady wind field reconstruction, the methods presented in this paper provide a solution for reconstruction of an unsteady wind field, especially for completely unknown incoming flows, greatly enhancing the practical application value of wind field reconstruction in short-term wind prediction. In the wind power industry, the presented methods can be used in the wind energy resource evaluation, wind turbine performance diagnosis, and optimization of wind turbine arrangements.

2. Numerical Reconstruction Method Based on Reduced-Order Model

2.1. Two-Dimensional Reconstruction Based on Snapshot POD

As a batch data processing method, Proper Orthogonal Decomposition (POD) involves applications in many fields, e.g., weather forecasting, image recognition, number analysis, data compression, stochastic processes and oceanography [36]. In the study of the turbulent velocity field, POD can associate the coherent structure with the energy contained in it to identify the structure of various energy levels in the turbulent flow field. Lumley [37] first introduced POD into the turbulent flow field in 1967. Sirovich [38] improved the direct POD method proposed by Lumley and proposed a snapshot POD method (Snapshot POD), which solved the difficult problem of a huge spatial matrix and made it possible for the

POD method to deal with a complex flow field, thus greatly promoting the study of a coherent structure in turbulent flow fields.

Considering the complexity of the flow field in this study, the basic principle of snapshot POD is described below.

If it is supposed that there are m discrete sampling points in space, $x_1, x_2 \ldots, x_m$, the values of m discrete points can be obtained by single sampling: $u_1(x_1), u_1(x_2), \ldots u_1(x_m)$. A total of N moments can then be collected to obtain the spatial field:

$$(u_1(x_1), u_1(x_2), \ldots u_1(x_m)), (u_2(x_1), u_2(x_2), \ldots u_2(x_m)), \ldots (u_N(x_1), u_N(x_2), \ldots u_N(x_m)) \quad (1)$$

which can be expressed as a matrix:

$$U = \begin{pmatrix} u_1(x_1) & u_2(x_1) & \cdots & u_N(x_1) \\ u_1(x_2) & u_2(x_2) & \cdots & u_N(x_2) \\ \vdots & \vdots & \vdots & \vdots \\ u_1(x_m) & u_2(x_m) & \cdots & u_N(x_m) \end{pmatrix} \quad (2)$$

Each column of matrix U is the value of all the spatial points acquired, i.e., the unsteady data of the entire field at a given time on the entire spatial point, which is called a snapshot. The time-dependent matrix can then be constructed as follows:

$$C = \frac{1}{m} U^T U \quad (3)$$

Then, the eigenvalues and eigenvectors of the time-dependent matrix can be obtained by eigenvalue decomposition:

$$CA = \lambda A \quad (4)$$

Thus, the characteristic functions can be constructed as follows:

$$\Phi = UA, \Phi = \{\phi_1, \phi_2, \ldots, \phi_N\} \quad (5)$$

Then, Φ is orthogonalized to obtain the POD mode, $\{\varphi_1, \varphi_2, \ldots, \varphi_N\}$, and φ_i is also called the basis vector. The modal coefficients corresponding to each mode can be calculated by the following formula:

$$a_i = U\varphi_i \quad (6)$$

Then, the original velocity field at any time can be reconstructed from the above POD modes and corresponding modal coefficients:

$$u^k(x) \approx \sum_{n=1}^{m} a_n^k \varphi_n(x) \quad (7)$$

It is worth noting that the above formula needs to be improved when the velocity field, at the moment of its reconstruction, is not in the database. Therefore, to deal with unknown velocity fields, the measurement matrix M, which is a 0–1 matrix, needs to be introduced.

$$M = [e_{\lambda 1}\ e_{\lambda 2} \cdots\ e_{\lambda r}]^T \quad (8)$$

where e_j represents the canonical basis vectors for $\mathbb{R}^n$ ($\mathbb{R}$ represents the real number) with a unit entry at index j and zeros elsewhere. M can be represented as follows:

$$M = \begin{bmatrix} 0 & 0 & \cdots & 1 & & & & \cdots & 0 \\ 0 & \cdots & 1 & 0 & 0 & \cdots & & \cdots & 0 \\ 1 & \cdots & 0 & 0 & \cdots & 0 & 0 & \cdots & 0 \\ \vdots & 0 & & & \cdots & 0 & 0\ 1 & \cdots & \vdots \\ 0 & \cdots & & 0 & \cdots & 1 & 0\ 0 & \cdots & 0 \end{bmatrix} \quad (9)$$

The matrix M defines a projection onto an r-dimensional space y that can be used to approximate solutions of $u^k(x)$.

$$y_i = \sum_{j=1}^{m} M_{ij} u_j^k(x) = \sum_{j=1}^{m} M_{ij} a_j^k \varphi_j(x) \tag{10}$$

The corresponding modal coefficient a can be determined with the Moore–Penrose pseudoinverse. Subsequently, the reconstruction of $u^k(x)$ can be obtained using:

$$\hat{u}^k(x) = \Phi a, \text{ where } a = \Theta^{\dagger} y = (M\Phi)^{\dagger} y \tag{11}$$

Finally, the relative error was defined by the L-1 norm to represent reconstruction accuracy:

$$RE = \frac{\left\| u^k(x) - \hat{u}^k(x) \right\|_1}{\|u\|_1} \times 100\% \tag{12}$$

Obviously, the foundation for the reconstruction using POD is the establishment of a matrix database, but when the three-dimensional space and time domain are combined, the concept of the tensor needs to be introduced to construct the tensor database of the wind field.

2.2. Three-Dimensional Reconstruction Based on Tensor Decomposition

With the diversity of data sources, the amount of data also increased. It is an effective method to represent large data by a tensor model and to process large data by means of tensor decomposition. Common tensor decomposition methods include CP decomposition [39], Tucker decomposition [40], HOSVD decomposition [41], and TT decomposition [42]. In this section, an efficient method based on Tucker decomposition is proposed for the rapid reconstruction of a three-dimensional wind field.

Tucker decomposition was proposed by Tucker in 1966 and is similar to CP decomposition in that it decomposes tensors into smaller core tensors and factor matrices. Tucker's definition of decomposition is as follows:

$$\begin{cases} \chi \approx \sum_{r_1}^{R_1} \cdots \sum_{r_N}^{R_N} a_{r_1 r_2 \ldots r_N} b_{r_1}^1 \circ b_{r_2}^2 \circ \cdots \circ b_{r_N}^N = A \times_1 B_1 \times_2 B_2 \times \cdots \times_N B_N \\ vector(\chi, 1) = A \overline{\times}_1 (B_N \otimes B_{N-1} \cdots \otimes B_1) \end{cases} \tag{13}$$

where $a_{r_1 r_2 \ldots r_N}$ represents the element of core tensor A and $A \in \mathbb{R}^{R_1 \times R_2 \cdots \times R_N}$, $B_N = \left[b_1^n, b_2^n, \cdots b_{R_n}^n \right] \in \mathbb{R}^{I_n \times R_n}$ represents the factor matrix, $vector(\chi, 1)$ represents the 1-mode vector form of tensor χ, and $\overline{\times}_1$ represents the 1-mode tensor-vector product. Figure 1 is an illustration of Tucker's decomposition for a third-order tensor.

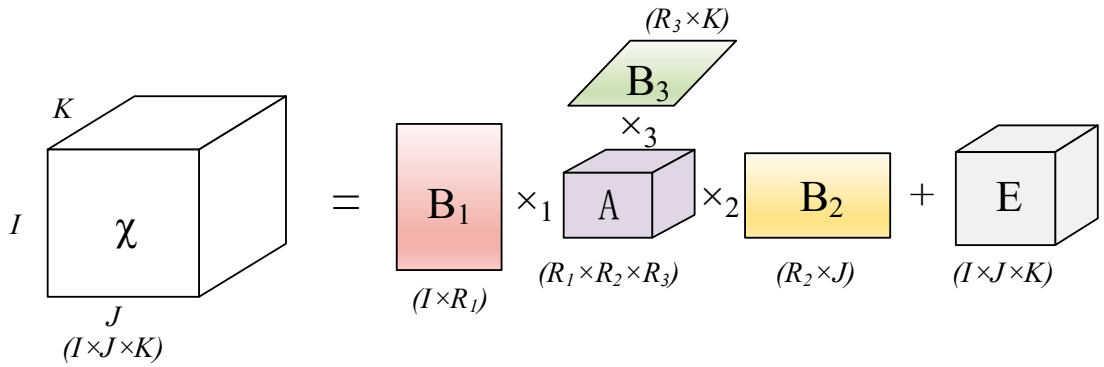

Figure 1. Illustration of Tucker decomposition for a third-order tensor.

As mentioned in Section 2.1, the discrete wind speed value can be measured by the constructed measurement matrix P and is represented by Y. Referring to Equation (10), the relationship between measurements and sensor locations can be expressed as:

$$Y = P \times v^k(x) \tag{14}$$

Referring to Equation (7), the 3D velocity field to be reconstructed can be considered as a linear combination of modes and their corresponding modal coefficients:

$$v^k(x) \approx \sum_{n=1}^{m} \beta_n^k \psi_n(x) \tag{15}$$

From the theoretical deduction in Section 2.1, it can be seen that the calculation process of POD is relatively simple; only the eigenvalue solution and matrix transformation are needed, without involving iterative calculation, which results in relatively simple calculation and easy implementation of POD [43]. However, unlike POD, the common solution of Tucker decomposition is ALS (Alternating Least Squares), which is an iterative decomposition algorithm based on collaborative filtering [44]. Therefore, the solution of modes in Tucker decomposition is more complex and time-consuming than POD. Firstly, the 4D tensor database $V \in R^{n_1 \times n_2 \times n_3 \times N}$ needs to be decomposed according to Equation (13):

$$V = \{V_1, V_2, \ldots, V_i, \ldots, V_N\} = A \times_1 B_1 \times_2 B_2 \times_3 B_3 \times_4 B_4 \tag{16}$$

Additionally, the B_4 can be shown as follows:

$$B_4 = \{b_1, b_2, \ldots, b_i, \ldots, b_N\} \tag{17}$$

where b_i is the i-th vector in the B_4, $b_i \in \mathbb{R}^{R_4 \times 1}$. Combining Equation (16) with Equation (17) yields:

$$V = \{V_1, V_2, \ldots, V_i, \ldots, V_N\} = A \times_1 B_1 \times_2 B_2 \times_3 B_3 \times_4 \{b_1, b_2, \ldots, b_i, \ldots, b_N\} \tag{18}$$

Obviously, the V_i can be obtained by the following equation:

$$V_i = T \times_4 b_i \tag{19}$$

where T is the Tucker mode tensor, $T = A \times_1 B_1 \times_2 B_2 \times_3 B_3$.

Up to now, similar models in POD seem to have been found, but their solution is slightly more complex. Therefore, the 3D wind speed distribution at k-moment $v^k(x)$ can be represented by the above equation, which is:

$$v^k(x) = T \times_4 b \tag{20}$$

Expanding the tensor T according to the fourth modulus yields:

$$v^k(x) = T^T{}_{4unfold} \times b \tag{21}$$

Notably, the $T^T{}_{4unfold}$ is a matrix, which can be combined with the measurement matrix P according to Equation (14):

$$Y \approx PT^T{}_{4unfold} b \tag{22}$$

Up to now, the reconstruction of the 3D wind field has also been converted into the solution of the modal coefficient b, which can be solved according to Equation (11). Once b is obtained, $v^k(x)$ can be calculated by Equation (21). Finally, the metric of the reconstruction accuracy is also defined by the L-1 norm according to Equation (12). Significantly, for 2-D and 3-D wind field reconstruction calculations, if the relative reconstruction error of

absolute velocity is less than 0.1%, the reconstruction calculation is considered convergent and the reconstruction results are excellent.

The most prominent feature of the two algorithms mentioned above is that the undetermined problem can be transformed into over-determined equations through matrix and tensor decomposition. Finally, it can be easily solved by the Moore–Penrose pseudoinverse, which not only saves computing time but also greatly improves the accuracy of reconstruction.

3. Reconstruction Results Based on CFD Wind Field Database

3.1. Construction of Simulated Wind Field Environment

To validate the reliability of the proposed methods in unsteady complex wind fields, a wind tunnel model with a complex terrain was simulated using hemispherical and sinusoidal models. Figure 2 shows the isometric diagrams of the wind tunnel in detail. Additionally, Figure 3 shows the specific dimensions of the geometric model and wind tunnel. The wind speed at the entrance of the wind field could be considered uniformly distributed, and the wind direction was defined as the angle between the wind speed direction and the positive half-axis of the X-axis.

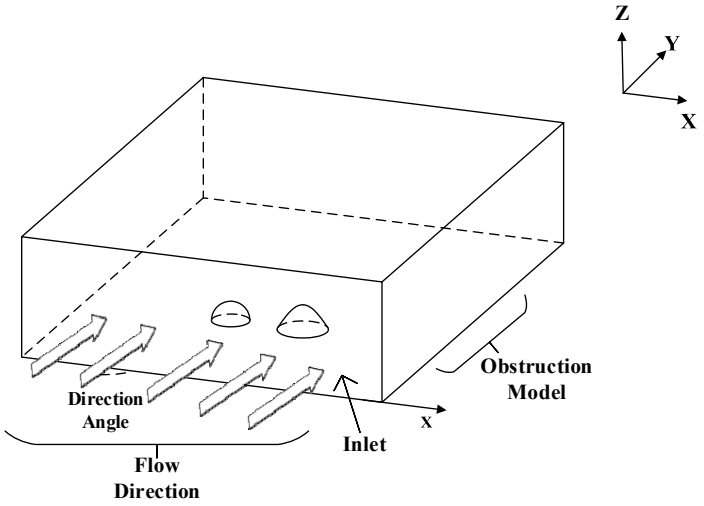

Figure 2. Geometric model of the simulated wind field environment.

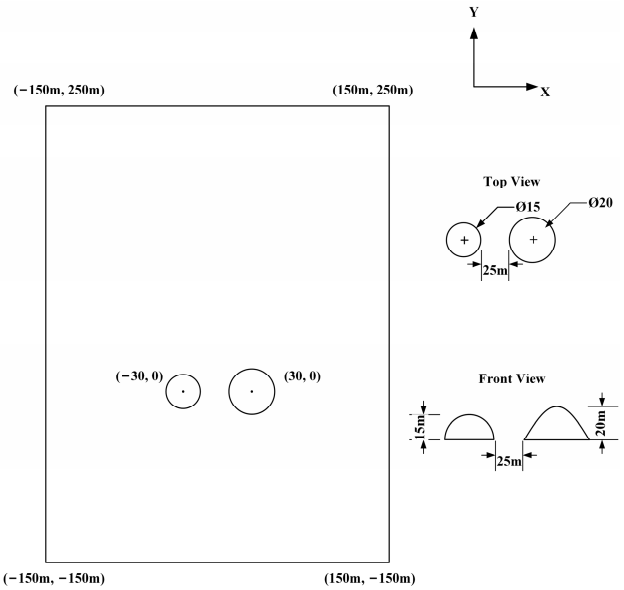

Figure 3. Dimensional diagram of the geometric model.

The specific dimensions of the analyzed spaces are shown in Figure 3, with a length of 400 m, a width of 300 m, and a height of 100 m. In addition, a simulated mountainous environment consisting of obstacle models is shown in the figure. The bottom radius and height of the hemisphere was 15 m, and the bottom center coordinate was (−30 m, 0 m). The sinusoidal model was formed through the rotation of a sinusoidal curve around the central axis, with a bottom radius of 20 m, and the center position of the bottom was symmetrical with the hemisphere along the y-axis. The distance between the sinusoidal model and the hemispherical model was 25 m.

3.2. Construction of Simulation Database

In this study, the most critical step was the establishment of a wind speed database, from which sufficient database information can ensure accurate feature extraction. In this paper, the two-dimensional wind speed distribution was represented by the plane above the model, and the 3D space of the area was expressed by five stacked planes. As described in Sections 2.1 and 2.2, the wind speed distribution simulated by CFD with different inlet wind speeds were stored in the matrix database U and the 4-D tensor database V, respectively. A continuity equation and momentum conservation equation were used to simulate the velocity distribution of the wind fields. The corresponding equations are as follows:

Continuity equation:

$$\frac{\partial \rho}{\partial t} + \frac{\partial (\rho u_x)}{\partial x} + \frac{\partial (\rho u_y)}{\partial y} + \frac{\partial (\rho u_z)}{\partial z} = 0 \tag{23}$$

Momentum equation:

$$\begin{cases} \frac{\partial \rho u_x}{\partial t} + \rho\left(u_x \frac{\partial u_x}{\partial x} + u_y \frac{\partial u_x}{\partial y} + u_z \frac{\partial u_x}{\partial z}\right) = \rho F_x - \frac{\partial p}{\partial x} + \mu\left(\frac{\partial^2 u_x}{\partial x^2} + \frac{\partial^2 u_x}{\partial y^2} + \frac{\partial^2 u_x}{\partial z^2}\right) \\ \frac{\partial \rho u_y}{\partial t} + \rho\left(u_x \frac{\partial u_y}{\partial x} + u_y \frac{\partial u_y}{\partial y} + u_z \frac{\partial u_y}{\partial z}\right) = \rho F_y - \frac{\partial p}{\partial y} + \mu\left(\frac{\partial^2 u_y}{\partial x^2} + \frac{\partial^2 u_y}{\partial y^2} + \frac{\partial^2 u_y}{\partial z^2}\right) \\ \frac{\partial \rho u_z}{\partial t} + \rho\left(u_x \frac{\partial u_z}{\partial x} + u_y \frac{\partial u_z}{\partial y} + u_z \frac{\partial u_z}{\partial z}\right) = \rho F_z - \frac{\partial p}{\partial z} + \mu\left(\frac{\partial^2 u_z}{\partial x^2} + \frac{\partial^2 u_z}{\partial y^2} + \frac{\partial^2 u_z}{\partial z^2}\right) \end{cases} \tag{24}$$

where ρ is the fluid density, u_x, u_y, and u_z are the velocity component at coordinates (x, y, z) at time t, respectively. p is the pressure, and ρF is the unit mass force. μ is the dynamic viscosity. Although the three-dimensional transient Navier-Stokes equation can be used to describe turbulence, its non-linear application cannot accurately describe the time-dependent fluid change characteristics. In engineering applications, turbulence is the main factor causing the change of mean flow field and more complex models are needed to describe the overall flow effect. Therefore, the turbulent model based on Reynolds averaging Navier-Stokes (RANS) equations is required to solve the flow field. In RANS, the instantaneous velocity values are decomposed into time-averaged velocity and fluctuation components.

$$u_i = \overline{u_i} + u_i' \tag{25}$$

The above equation is substituted into the continuity equation and momentum equation for time-averaged calculation, and the continuity equation and momentum equation for time-averaged flow are obtained:

Continuity equation:

$$\frac{\partial \rho}{\partial t} + \frac{\partial}{\partial x_i}(\rho u_i) = 0 \tag{26}$$

Momentum equation:

$$\frac{\partial u_i}{\partial t} + u_j \frac{\partial u_i}{\partial x_j} = f_i - \frac{1}{\rho}\frac{\partial p}{\partial x_i} + \frac{\partial}{\partial x_j}\left[v\left(\frac{\partial u_i}{\partial x_j} + \frac{\partial u_j}{\partial x_i}\right) - \overline{u_i' u_j'}\right] \tag{27}$$

In order to close the control equation, the number of additional turbulent flows introduced needs to be the same as the number of additional differential equations solved.

According to the number of additional differential equations solved, eddy viscosity modes can generally be divided into four categories: zero equation mode, half equation mode, one equation mode, and two equation mode. The standard $k-\varepsilon$ model in the two-equation model is widely used in engineering flow field calculations due to its advantages of wide applicability, low computational cost, and reasonable accuracy.

For boundary conditions, the inlet type was chosen to be the 'velocity-inlet', and prepared UDF was imported, with the outlet set to the 'pressure-outlet'. Referring to previous CFD calculations on slip conditions and cavitation, since the wind field above 20 m above the obstacle model is considered in this paper, which is beyond the scope of the boundary layer and does not involve the wind speed distribution around the wall, neither the obstacle model nor the wind tunnel wall in this study involves slip and cavitation [45]. Moreover, the turbulence intensity and viscosity ratio of the inlet were set to 5% and 10%, respectively.

In this study, wind field databases were constructed with different inlet boundary conditions, and the sine equation was used to define the variation in the inlet speed with time:

$$v = v_0 + 2\sin(\pi t) \tag{28}$$

where v is the inlet speed and v_0 is the initial speed. The velocity was assumed to be uniform in the inlet section. Based on the above equation, the difference in the inlet speed was mainly reflected by two aspects: a different initial speed and a different inlet angle. Therefore, in this study, the wind speed database was constructed by changing the initial speed and the inlet angle. Three groups of the initial velocity and incident angle were set at inlet boundary conditions, which were 5 m/s, 45°; 10 m/s, 90°, and 15 m/s, 135°, respectively.

In the CFD calculation, the time step was set to 0.1 s; in total, 500-time steps were set, and the data were saved once at every 0.2 s interval. After the calculation was complete, the wind velocity distribution in the 8 s–16 s time interval of 41 moments was selected to form a database under boundary conditions. Finally, the three databases were combined into a complete wind field database. The dimensions of the matrix database U could be represented as $n \times N$, where n represented the selected measurement points, and N was the number of snapshots. The values of n and N were 10,000 (100 points in the x-direction and 100 points in the y-direction) and 123, respectively. The selected plane was 22 m high and 120 m × 100 m in size. In addition, the dimensions of the tensor database V were $n_1 \times n_2 \times n_3 \times N$, where n_1 and n_2 represented the measurement points selected along the X and Y direction, respectively, while n_3 and N represented the number of selected planes and snapshots, respectively. The values of n_1, n_2, n_3 and N were 100, 100, 5, and 123, respectively. The five planes were 22 m, 25 m, 30 m, 35 m, and 40 m in height and 120 m × 100 m in size. The reconstruction results and error analysis were based on the two databases.

3.3. CFD Calculation

Before the reconstruction calculation, two important preparations needed to be completed: mesh division and fluent parameter setting.

The meshing strategies used in CFD calculations can be roughly divided into two categories: structured meshing and unstructured meshing. The characteristic of structured meshing is that the connection relationship between each node and adjacent points is fixed and implicit in the generated grid, so it is not necessary to specifically set data to confirm the relationship between nodes and adjacent points. The main advantages of structured meshing are as follows: (1) Fast generation of a grid; (2) the quality of the generated grid is good; (3) the data structure is simple; (4) most fitting methods for surface or space removal are parameterized or spline interpolation, and the area is smooth and closer to the actual model; (5) it is easy to achieve the boundary fitting of the region, which is suitable for the calculation of fluid field. Unstructured grid generation technology is mainly used to compensate for the lack of structured grids that cannot solve the mesh

generation of arbitrary shapes and connected regions. However, the generation technology of unstructured grids is relatively complex, and currently only the automatic generation technology of planar triangles is relatively mature. The structure of the wind tunnel model in this study is relatively simple, and the geometric shape of the obstacle model is relatively regular. In structured meshing strategies, quadrilateral meshes are generally used for two-dimensional geometry and hexahedral meshes for three-dimensional geometry. Therefore, the hexahedral structured mesh is chosen as the meshing strategy, and the mesh generation tool is ICEM CFD. The mesh was encrypted around the models and boundary, and "o-block" was performed near the hemispherical and sinusoidal models. The partitioned locally encrypted hexahedral structured grid and boundary layer grid are shown in Figure 4.

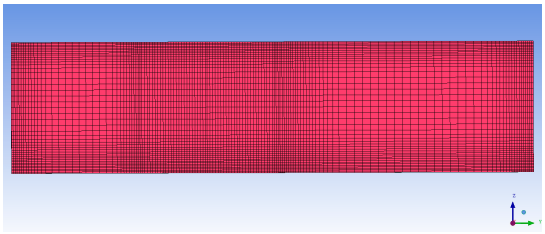

(**a**) Wall boundary mesh

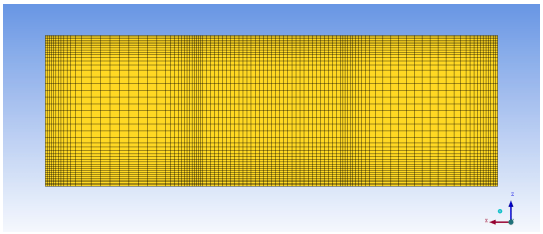

(**b**) Inlet boundary mesh

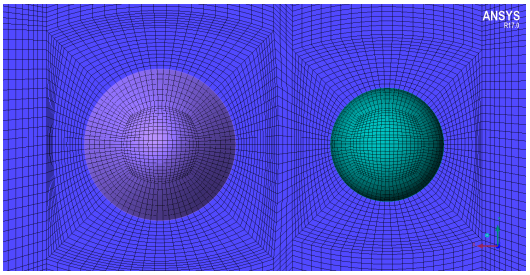

(**c**) Encrypted mesh around models

Figure 4. Local mesh refinement for the wind tunnel.

In addition, the mesh independence test is crucial in the mesh division. The mesh independence test can be stated as a mesh convergence study obtained through identical models with different elements, including coarse elements (small number of elements) and fine elements (large number of elements) [46]. It aims to select computational models with an optimal number of elements, and not too many, in order not to burden the computational load whilst still being able to provide accurate results [47,48]. In the mesh independence test, 2,694,420 units were considered the standard. For comparison, three dense-to-sparse grids were designed: 1,133,561, 546,184, and 22,385. Five planes with 50,000-speed values were selected for comparison. The relative errors between the calculated speed values of the three groups of mesh and those of 269,420 units are shown in Table 1. Obviously, when the number of units reached 546,184, the relative error decreased to about 0.3%. If the number of units increased to 1,133,561, the error could be further reduced, but the calculation cost would still be multiplied. Therefore, considering both the accuracy and time cost, 546,184 elements were selected for fluent calculation. The corresponding number of nodes and edges is 571,284 and 194, respectively.

Table 1. Mesh independence test.

Mesh Number	Relative Error (%)
223,875→546,184	0.59
546,184→1,133,561	0.36
1,133,561→2,694,420	0.21

After importing the drawn mesh into the fluent, the calculation parameters were set in detail as follows: The 'Pressure-Based' method and 'Unsteady' were selected as the solver. The solution method and gradient were chosen as 'PISO' and 'Least Squares Cell Based', respectively. Momentum, turbulent kinetic energy, and turbulent dissipation rate were all selected as the 'Second-Order Upwind'. The time step was set to 0.1 s; in total, 500-time steps were set, the case and data were automatically saved once at every 0.2 s interval, and the convergence residuals were set to 1×10^{-3}. Finally, to determine an appropriate turbulence model, three boundary conditions and five typical turbulence models (standard K-ω, SST K-ω, realizable K-ε, RNG K-ε and standard K-ε) are selected. Based on the standard K-ε, the calculation results of the other four models at 18.6 s are shown in Table 2. It can be concluded from Table 2 that the calculation results of the five models are very similar. However, standard K-ε has the advantages of low computational requirements, strong computational stability and fast convergence speed. Thus, standard K-ε was chosen as the viscous model.

Table 2. Relative errors compared with "Standard K-ε".

Boundary Conditions	Realizable K-ε	RNG K-ε	Standard K-ω	SST K-ω
13 m/s, 130°	0.62%	0.76%	0.81%	0.94%
8 m/s, 90°	0.37%	0.51%	0.47%	0.83%
17 m/s, 150°	0.29%	0.55%	0.64%	0.70%

3.4. Presentation of Reconstruction Results

After the construction of the wind field database was complete, the two-dimensional and three-dimensional wind fields were reconstructed using the database in this section. To verify the reliability of the reconstruction methods, three boundary conditions were designed to validate the reconstruction, which were: 13 m/s, 30°; 8 m/s, 90°; and 17 m/s, 150°. The wind speed distribution at 18.6 s was selected as the reconstruction validation and result presentation. The reconstruction results were presented mainly from a comparison between the reconstructed nephograms and the CFD nephograms, as well as the reconstruction error of the three boundary conditions.

Summarizing the two reconstruction methods, the number of basis vectors and the dimension of core tensor, the number of sensors and the sensor measurement noise need to be determined before calculation. The number of basis vectors was determined to be 10, and the core tensor dimensions were set to [10, 10, 5, 10]. To facilitate the display of sensor locations in nephograms, 20 sensor data were selected as measurements in this study, which only accounted for 0.2% and 0.04% of the total data of the 2D and 3D wind fields, respectively. Finally, the measurement noise γ was defined by Gaussian noise:

$$\gamma \sim N\left(0, \sigma^2\right) \tag{29}$$

Here, σ is the standard deviation, and N is the normal distribution function in relation to σ^2, and the noise level can be defined by σ:

$$Noise\_level = \sigma \times 100\% \tag{30}$$

The noise level was set to 10% in this section. To ensure accurate results, 1000 calculations were performed for each reconstruction to obtain an average. In this section, the results of the reconstruction are presented to preliminarily verify the feasibility of the proposed method. The factors affecting reconstruction accuracy are discussed in the next section.

After determining the relevant calculation parameters, the velocity nephograms and the relative reconstruction error were obtained by calculation. In this study, the reconstruction errors of the absolute velocity $\boldsymbol{u}$ and the component velocity in three directions, i.e., the component velocity $\boldsymbol{u_x}$ in the X direction, the component velocity $\boldsymbol{u_y}$ in the Y direction, and

the component velocity u_z in the Z direction, are shown. As a representative, the two- and three-dimensional nephograms of the absolute velocity under three boundary conditions are shown.

Figures 5a–f and 6a–c show the 2D and 3D nephograms of reconstructed and simulated velocity distribution, respectively. The reconstructed nephograms in Figure 5 can clearly restore the distribution characteristics of wind speed, and the range of velocity variation is highly consistent with the preset CFD wind field. In addition, it can be seen from Figure 6 that the 20 sensors were uniformly distributed on five planes, and the reconstructed nephograms obtained were highly consistent with the nephograms calculated by CFD. Notably, in order to ensure the reliability of the reconstruction results, the sensor locations under the three boundary conditions were fixed during the reconstruction process.

A large number of nephograms in Figures 5 and 6 have preliminarily validated the reliability of the two reconstruction methods. Tables 3 and 4 further explore the accuracy of reconstruction in different dimensions and the reconstruction errors of different velocity components. Four conclusions can be drawn by analyzing the reconstruction errors in Tables 3 and 4: (1) The reconstruction errors of absolute velocity with the three boundary conditions are quite low (all lower than 0.8%). It is important to note that only 20 measurements were available that fully proved the reliability of the two reconstruction methods in their respective application fields. (2) In 2D and 3D reconstruction, the error of u_z was the largest, since the absolute value of u_z was too small, which resulted in the inaccurate feature extraction of u_z database. (3) The reconstruction error in the X-direction of the boundary condition 8 m/s, 90° was generally large since the component velocity in the X direction was small when the incidence angle of the wind was 90°; this is similar to the reason analyzed in conclusion 2. However, simulated wind fields are often idealized, whereas the wind direction in the real wind field environment is random, and a completely vertical wind direction angle does not exist. (4) The amount of reconstructed data for the 3D wind field was five times that of the 2D wind field, but the error of absolute speed was lower. This proves the superiority of Tucker's decomposition when dealing with high-dimensional data and illustrates the importance of efficient feature extraction when solving inverse problems.

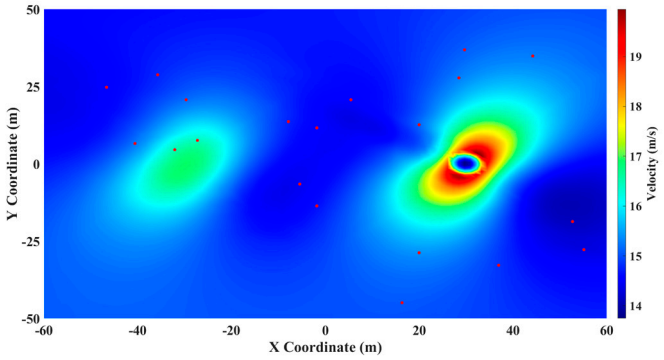

(**a**) Nephogram for CFD simulation (13 m/s, 30°)

Figure 5. *Cont.*

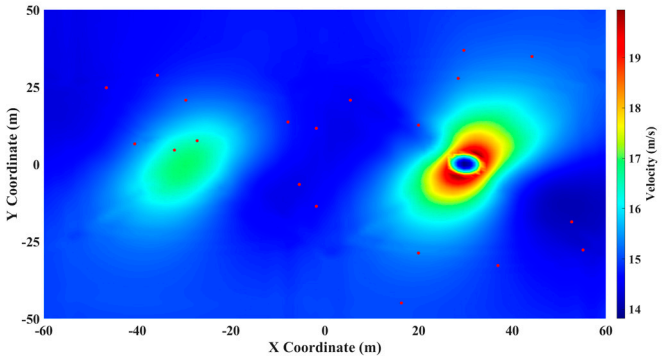

(**b**) Nephogram for reconstruction (13 m/s, 30°)

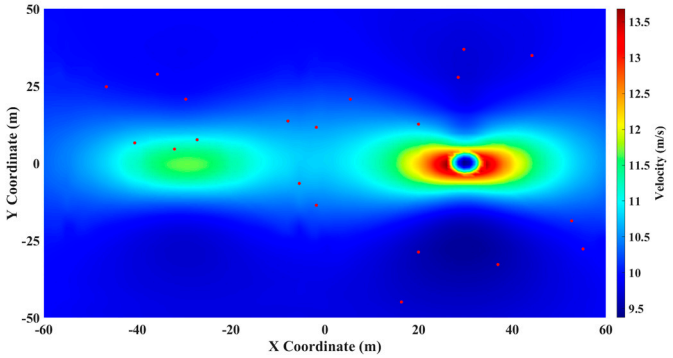

(**c**) Nephogram for CFD simulation (8m/s, 90°)

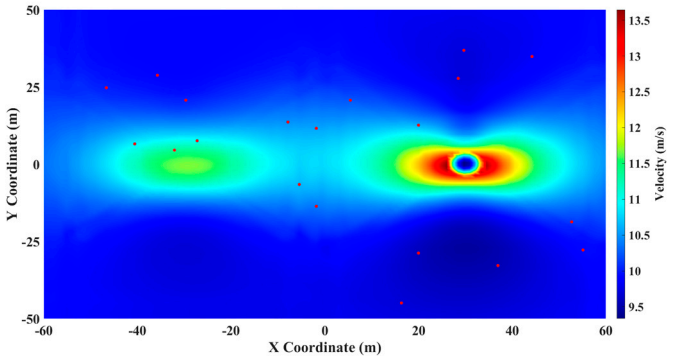

(**d**) Nephogram for reconstruction (8 m/s, 90°)

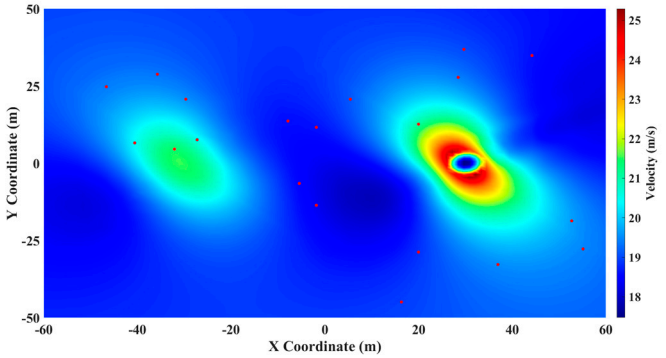

(**e**) Nephogram for CFD simulation (17 m/s, 150°)

Figure 5. *Cont*.

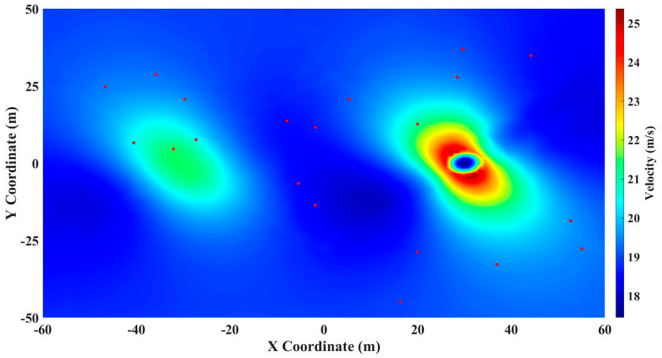

(**f**) Nephogram for reconstruction (17 m/s, 150°)

Figure 5. CFD and reconstruction nephograms with sensor locations (red dot) at 18.6 s under three boundary conditions (POD).

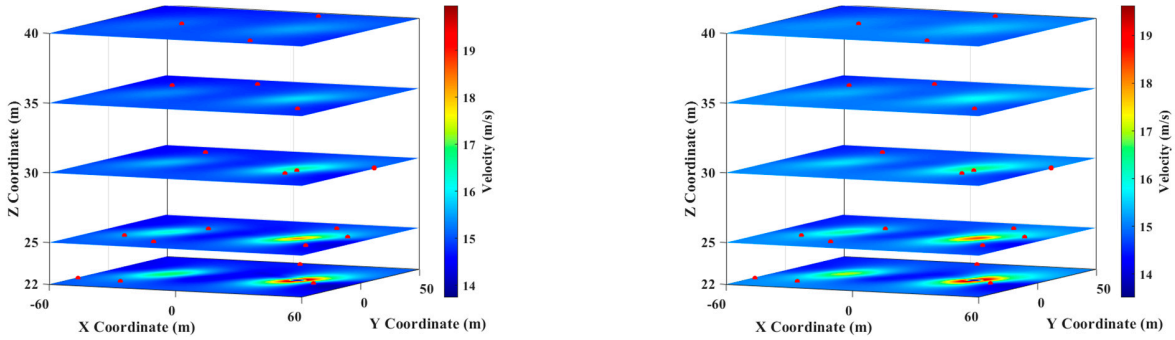

(**a**) Nephogram for boundary condition 13 m/s, 130°

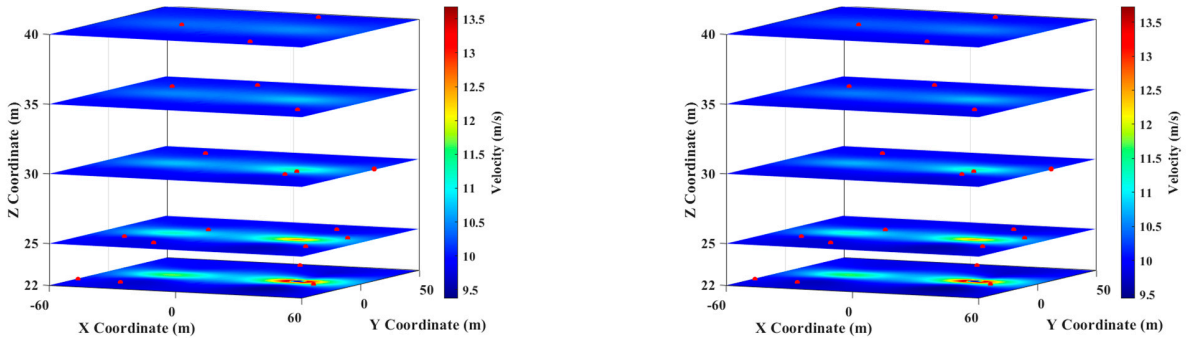

(**b**) Nephogram for boundary condition 8 m/s, 90°

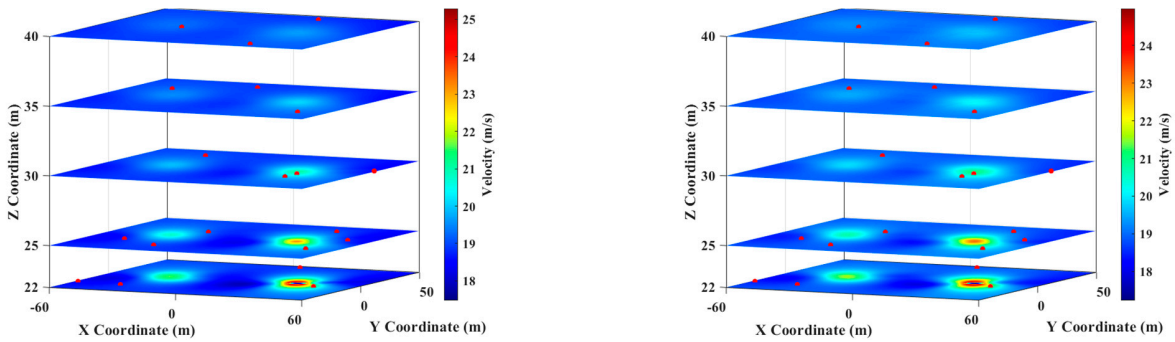

(**c**) Nephogram for boundary condition 17 m/s, 150°

Figure 6. Nephograms of CFD (left) and reconstruction (right) with sensor locations (red dot) at 18.6 s under three boundary conditions (Tucker decomposition).

Table 3. Reconstruction error (%) of absolute velocity and velocity component under three boundary conditions (POD).

Velocity	Boundary Condition		
	13 m/s 130°	**8 m/s 90°**	**17 m/s 150°**
u	0.62	0.76	0.45
u_x	0.84	37.53	1.29
u_y	1.31	0.81	1.02
u_z	29.44	24.23	23.61

Table 4. Reconstruction error (%) of absolute velocity and velocity component under three boundary conditions (Tucker decomposition).

Velocity	Boundary Condition		
	13 m/s 130°	**8 m/s 90°**	**17 m/s 150°**
u	0.48	0.68	0.40
u_x	0.68	62.25	0.83
u_y	1.16	0.81	0.95
u_z	30.36	30.31	25.40

In this section, the applications of the two reconstruction methods in two-dimensional and three-dimensional unstable wind field reconstruction are verified by computational simulation. Although computational simulation research is the basis/preliminary study before experimental studies, such research has the advantages of lower cost and faster results compared with experimental testing [49–51]. However, it should be acknowledged that the lack of independent experimental validation is the limitation of the present study and it would be more convincing if the present study could be validated by performing an independent experimental study or by comparing with previous experimental/identical studies [52–54]. In general, the comparison of nephograms validated the fact that the proposed methods could accurately restore the distribution characteristics of the wind field. Moreover, from the error analysis, it can be concluded that although the reconstruction errors of the multi-dimensional wind field and multi-component velocity are different, the variation in errors was similar, and the reconstruction results of absolute velocity were excellent, which fully verifies the reliability of the proposed method for the fast and accurate reconstruction of 2D and 3D wind fields based on sparse sensors.

4. Discussion and Analysis

The results in the previous section are based on fixed solution conditions, e.g., the number of basis vectors, the 4-mode dimension of the core tensors, the noise level, the database dimensions, etc. In this section, the factors affecting the reconstruction results are systematically analyzed to improve the reconstruction accuracy of both methods.

4.1. Presentation of Reconstruction Errors at All Time Steps

In Section 3.4, only the characteristics of wind speed distribution and reconstruction errors at 18.6 s are shown. Therefore, before discussing the factors influencing the reconstruction results, this section first reconstructs the wind field distribution at all times (i.e., from 16.2 s to 20 s) and integrates the reconstruction errors.

Figures 7a–c and 8a–c show the relative error of u, u_x, u_y, and u_z with three boundary conditions using POD and Tucker. Both figures are double Y-axis diagrams, from which the following conclusions can be drawn:

(1) Under different boundary conditions, the reconstruction results of absolute velocity and the X-direction component velocity are satisfactory, but the reconstruction results of the Y-direction and Z-direction are poor, mainly because the absolute values of component velocity in these two directions are too small, the distribution gradient is large, and the

wind of component direction almost only exists around the obstacle model, which brings great difficulty to the feature extraction of the database.

(2) By comparing the three figures in the same group, it was found that the result of speed reconstruction with the boundary condition (8 m/s 90°) was worse than the other boundary conditions, and the error fluctuated greatly with the change in the inlet speed. This was mainly due to the insufficient convergence of the fluent calculation results, thus affecting the quality of the built database, which showed the important role of the pre-calculated database quality in wind field reconstruction.

(3) By comprehensive comparison with Figures 7 and 8, the amount of reconstruction data processed by Tucker decomposition was larger, but the reconstruction effect for the absolute speed was better than POD. This is due to the fact that after rearranging the matrix database into tensors in multi-direction, multi-plane and multi-time order, the data between the dimensions were more closely connected, and the wind speed distribution characteristics, including spatial-temporal information correlation, could be obtained more effectively.

(4) Interestingly, the reconstruction error curves shown in the two figures show a strong periodicity with a period of approximately 2 s; this appeared to be inextricably linked with the inlet speed. Therefore, in order to explore the relationship between the inlet speed variation and error period, Figure 9 shows the curves of inlet speed over time with three boundary conditions. Comparing this with Figures 7–9, we found the distribution characteristics of the error period. The period of error variation was roughly the same as that of speed variation, but the period of the peak and trough was exactly the opposite, i.e., the reconstruction error decreased with increasing speed and increased with decreasing speed. Essentially, this conformed to the rule of physical field reconstruction based on the feature extraction method, i.e., the more stable and powerful the physical field was, the easier it was to be reconstructed efficiently.

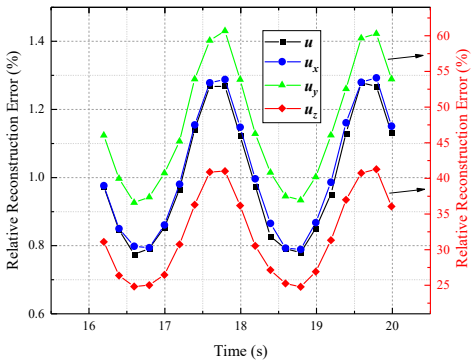

(**a**) Reconstruction error of absolute velocity and velocity component with boundary condition 8m/s 90°

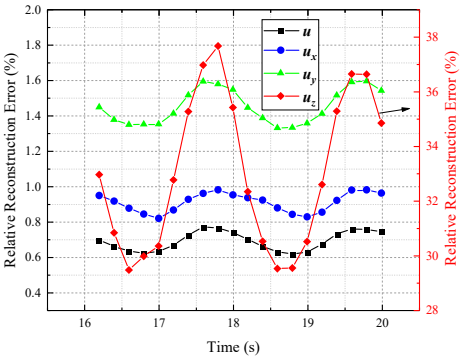

(**b**) Reconstruction error of absolute velocity and velocity component with boundary condition 13m/s 130°

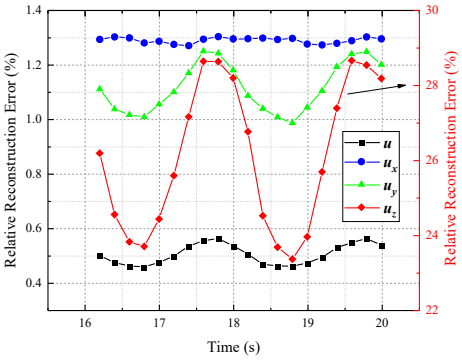

(**c**) Reconstruction error of absolute velocity and velocity component with boundary condition 17m/s 150°

Figure 7. Reconstruction error of absolute velocity and velocity component with three boundary conditions (POD).

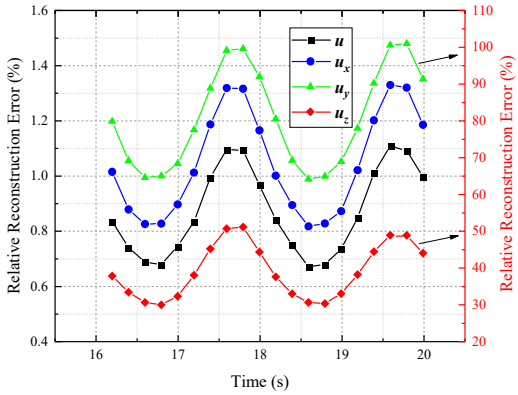

(**a**) Reconstruction error of absolute velocity and velocity component with boundary condition 8m/s 90°

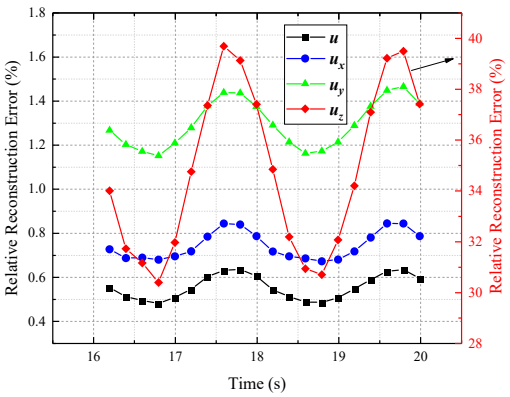

(**b**) Reconstruction error of absolute velocity and velocity component with boundary condition 13m/s 130°

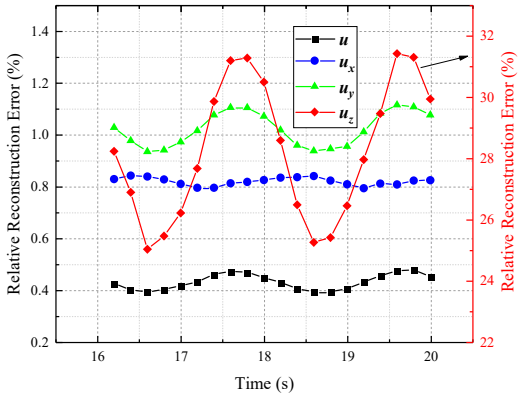

(**c**) Reconstruction error of absolute velocity and velocity component with boundary condition 17m/s 150°

Figure 8. Reconstruction error of absolute velocity and velocity component with three boundary conditions (Tucker decomposition).

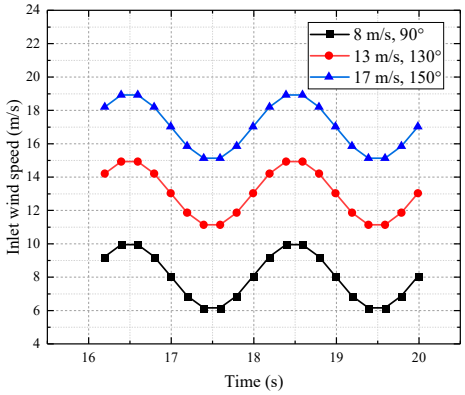

Figure 9. Inlet wind speed at all times from 16.2 s to 20 s.

4.2. Influence of Basis Vectors and Core Tensor Dimension on Reconstruction Performance

In the reconstruction calculation, the basis vectors and 4-mode dimensions had a profound impact on the calculation time and reconstruction accuracy, as it affected the solution of the modulus coefficient in Equations (11) and (22). Therefore, in this section, the number of basis vectors, 4-mode dimensions and noise level are combined to explore the reconstruction results under different conditions at 18.6 s to determine the optimal number of eigenvectors.

First, with fixed noise levels, the effects of the basis vectors and the core tensor dimension on the results need to be discussed. Notably, the reason behind choosing the

4-mode dimension for exploration is that it directly affects the dimension of the module coefficient $\boldsymbol{b}$, which, in turn, affects the reconstruction accuracy and computation time. In this section, the number of basis vectors and 4-mode dimensions was determined to be 1–20. The number of sensors was 20, and the noise level was 10%. Finally, the reconstruction error curves of POD and Tucker decomposition were obtained. As shown in Figure 10, when the noise level was fixed, the influence of this change in the basis vector and the 4-mode dimension on the error was almost the same. In addition, as the basis vector and 4-mode dimension increased, the reconstruction error decreased significantly, but when the dimension increased to five, the error showed an upward trend. This is because increasing the number of eigenvectors results in a higher dimension of Φ and T, while the eigenvectors corresponding to the minimum eigenvalue are usually associated with noise, so discarding it can significantly improve the reconstruction accuracy.

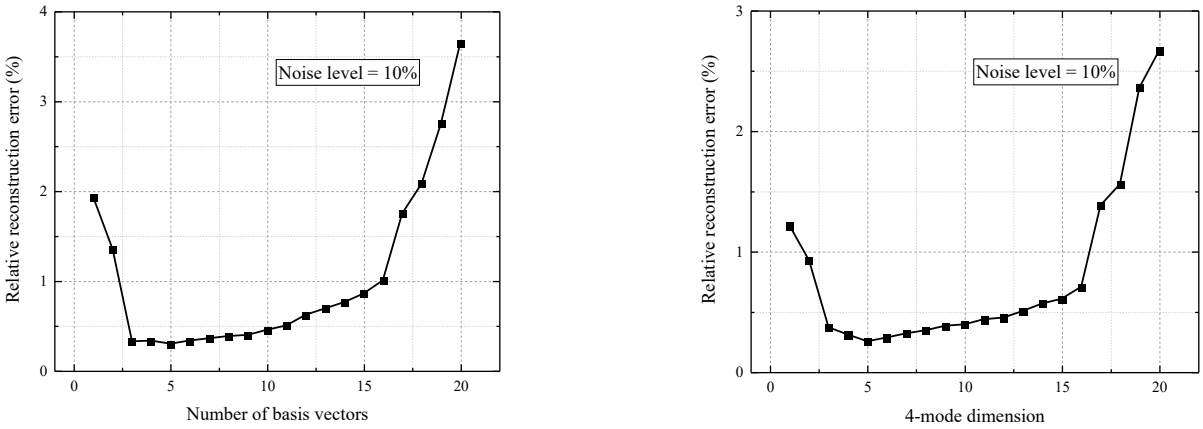

(**a**) POD (**b**) Tucker decomposition

Figure 10. Absolute velocity reconstruction errors (%) corresponding to a different number of basis vectors and 4-mode dimensions at 18.6 s (noise level is 10%).

After exploring the influence of different numbers of eigenvectors under the same noise level on the reconstruction error, it was necessary to further verify the robustness of the proposed reconstruction methods. In this section, the noise level increased from 1% to 20%, with an interval of 1%. Meanwhile, the number of basis vectors and 4-mode dimensions was set to 2, 4, 6, 8, and 10. It was assumed that noise only existed in the measurements and not in the pre-computed database, and the corresponding reconstruction error results are shown in Figure 11. From this, the following conclusions can be drawn:

Obviously, the relative reconstruction error increased significantly with the increase in the noise level. However, the error changed most smoothly when two eigenvectors were taken, although the error was the largest. Moreover, for larger 4-mode and basis vectors, the curve rose more sharply with the increase in the noise level. This feature illustrates that the reconstruction errors with larger basis vectors and 4-mode are more sensitive to noise, which confirms the conclusion of Figure 10. In addition, a turning point can be found in Figure 11, which shows that when the noise level is higher than 5%, larger basis vectors and 4-mode result in poorer reconstruction results, beyond which the effect of the eigenvectors on the errors reverses. In general, the increase in basis vectors and 4-mode dimensions was beneficial to the reconstruction result, but such an excessive increase may enable the reconstruction error to be more sensitive to noise. Notably, referring to Figure 11, when the measurement noise level was 10%, it appeared that the number of basis vectors and the 4-mode dimension should be determined to be six. Significantly, although the noise level reached 20%, the reconstruction error was still within an acceptable range (mostly below 1%). From this perspective, both reconstruction methods based on POD and Tucker decomposition had excellent noise resistance and could be regarded as a filter.

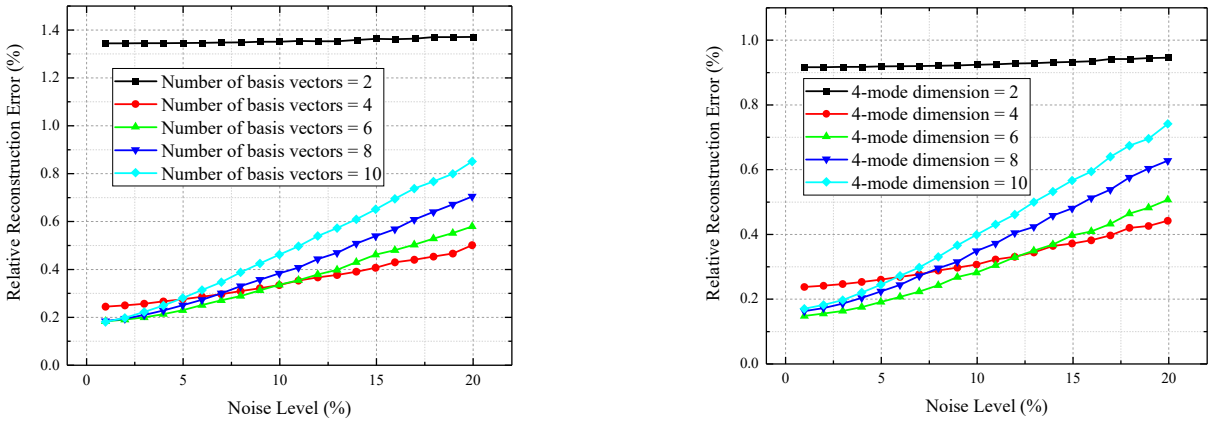

(**a**) POD (**b**) Tucker decomposition

Figure 11. Joint effect of the number of basis vectors, 4-mode dimensions and the noise level (%) on the reconstruction error of absolute velocity.

4.3. Influence of Simulation Database Construction on Reconstruction Performance

In the reconstruction calculation and error analysis of this paper, one critical factor has not been considered, i.e., the construction of a wind field database. In the simulation, data acquisition and database construction were easy to achieve, but in the actual wind field environment, due to the limitation of calculation time and measurement costs, an ideal wind field database was difficult to obtain. Therefore, at the end of this chapter, the impact of different database construction methods on the reconstruction error is discussed, which is of great significance for the application of the proposed reconstruction methods in the real wind field.

Based on the three different initial speed and incident angles set up in Section 3.2, five matrix databases and five tensor databases are outlined in this section. The construction principles are as follows: (1) The wind velocity distribution calculated by the three boundary conditions was taken as a database separately, and the two databases were named $U_i \in \mathbb{R}^{10000\times41}$ and $V_i \in \mathbb{R}^{100\times100\times5\times41}$, $(i = 1, 2, 3)$, respectively, in the order of 45°, 5 m/s, 90°, 10 m/s, and 135°, 15 m/s; (2). The wind speed distributions from 13.2 s to 16 s of the three databases were spliced together to form a low-dimensional version of the fused database, named $U_4 \in \mathbb{R}^{10000\times45}$, $V_4 \in \mathbb{R}^{100\times100\times5\times45}$; (3) All the calculated wind velocity distributions were sliced together to form a full-scale wind field database named $U_5 \in \mathbb{R}^{10000\times123}$, $V_5 \in \mathbb{R}^{100\times100\times5\times123}$. Then, based on the newly established five matrices and tensor databases, the reconstruction errors of absolute velocity at 18.6 s in the three boundary conditions were calculated using the proposed reconstruction methods. Notably, the number of sensors used in the calculation, the noise level, the basis vectors, and the 4-mode dimension were all in accordance with Section 3.4. Detailed calculation results are shown in Tables 5 and 6, and the following conclusions can be drawn:

(1) Obviously, the corresponding reconstruction results of the database with a single boundary condition were far inferior to that of the mixed database, which demonstrates the necessity of building multiple types of databases.

(2) By analyzing the reconstruction errors corresponding to U_1, U_2 and U_3, it was found that the wind direction angle had a higher influence on the reconstruction results than the initial velocity, i.e., the database features that were constructed needed to be as close to the actual wind field as possible to produce better reconstruction results.

(3) By comparing U_4 and U_5, it was found that the reconstruction errors based on a hybrid database and full-size database were almost the same, but the calculation time of the two databases was quite different (the calculation time based on U_5 is three times that of U_4), which indicates that in the wind field environment with prominent characteristics of wind speed distribution, the constructed database needs to contain rich speed distribution

information under different boundary conditions rather than multi-time data, so as to improve the reconstruction efficiency.

(4) Finally, by comprehensively comparing the reconstruction results of both tables, it was found that the reconstruction results based on Tucker's decomposition were significantly better than those based on POD, which proves the superiority of Tucker decomposition when extracting multi-dimensional tensor data features and demonstrates its lower dependence on the database.

Therefore, the following factors need to be considered: the wind speed distribution under multiple boundary conditions should be included as much as possible because the multi-category database construction has more advantages than the database with single-entry boundary conditions in the reconstruction calculation. Additionally, in the construction of a hybrid database, redundant database information needs to be removed in consideration of time costs.

Table 5. Absolute velocity reconstruction error (%) under three boundary conditions based on five different databases (POD).

Matrix Database	Boundary Condition		
	30°, 13 m/s	**90°, 8 m/s**	**150°, 17 m/s**
U_1	1.94	6.36	4.54
U_2	7.19	0.81	5.53
U_3	5.26	4.49	1.88
U_4	0.63	0.78	0.46
U_5	0.62	0.76	0.45

Table 6. Absolute velocity reconstruction error (%) under three boundary conditions based on five different databases (Tucker decomposition).

Tensor Database	Boundary Condition		
	30°, 13 m/s	**90°, 8 m/s**	**150°, 17 m/s**
V_1	1.14	3.31	5.15
V_2	3.68	0.94	2.61
V_3	2.86	1.82	0.83
V_4	0.52	0.73	0.42
V_5	0.48	0.67	0.39

At the end of this section, the reconstruction time with a different number of sensors based on POD and Tucker's decomposition was discussed, which was crucial for the reconstruction of the unsteady wind field. Based on the boundary condition 90°, 8 m/s, four groups of sensors (5, 10, 15, 20) were designed to discuss the time required for reconstruction, and the results are shown in Table 7. With the increase in the number of sensors, the time required for reconstruction also increased accordingly. In addition, since 3D wind data were five times larger than 2D wind data, the reconstruction time based on Tucker's decomposition was about five times that based on POD. When the number of sensors was compressed, such as five, the reconstruction time came close to 0.2 s and the time interval of data acquisition. This is of great significance in the reconstruction of the unsteady wind field. Because the reconstruction time can be further compressed when the computer performance is strong enough, it is possible to synchronize data acquisition with wind field reconstruction, which could promote the effective application of this method for short-term wind prediction.

Table 7. Reconstruction time (s) with a different number of sensors based on POD and Tucker decomposition.

Method	Sensor Number			
	5	**10**	**15**	**20**
POD	0.229	0.263	0.281	0.300
Tucker	0.962	1.153	1.336	1.517

4.4. Comparison of the Similar Methods

To further verify the superiority of POD and Tucker decomposition in wind field reconstruction, two existing reduced-order models are introduced: NMF (Nonnegative Matrix Factorization) [55] and HOSVD (Higher-Order Singular Value Decomposition) [56]. NMF is applied to the reconstruction of 2D wind speed distributions and compared with POD. The reconstruction result of HOSVD is compared with Tucker decomposition. Taking the three boundary conditions in Section 3.4 an example, the reconstruction errors of absolute velocity for the five methods are shown in Tables 8 and 9.

From Table 8, although both methods perform well in reconstructing absolute velocity, the relative reconstruction errors based on POD are the smallest. This is because although the principle of NMF is similar to POD, NMF is better at the non-negative matrix field in image processing, which guarantees that the extracted base vector is non-negative at the expense of losing some of the original information in the database. Therefore, POD is more advantageous in controlling the error of two-dimensional wind field reconstruction. From Table 9, the reconstruction results obtained by Tucker decomposition are significantly better than those obtained by HOSVD. This is because HOSVD is more difficult to control decomposition accuracy in tensor decomposition. In addition, the computational complexity of HOSVD is significantly higher than Tucker decomposition, which requires more time costs. Tucker decomposition has advantages over HOSVD in both calculation accuracy and time cost, so it is more suitable for reduced-order calculation of a wind field database. In general, the superiority of POD and Tucker decomposition in 2-D and 3-D wind field reconstruction is verified by comparing the reconstruction errors of similar reduced-order models.

Table 8. Comparison of relative reconstruction errors (%) of POD and NMF.

Methods	Boundary Condition		
	30°, 13 m/s	**90°, 8 m/s**	**150°, 17 m/s**
POD	0.62	0.76	0.45
NMF	1.07	1.35	1.09

Table 9. Comparison of relative reconstruction errors (%) of Tucker decomposition and HOSVD.

Methods	Boundary Condition		
	30°, 13 m/s	**90°, 8 m/s**	**150°, 17 m/s**
Tucker	0.48	0.68	0.40
HOSVD	1.16	1.47	1.15

5. Conclusions

In the present paper, two innovative wind field reconstruction methods combining CFD and reduced order model were explored based on a tailored library of features extracted from the matrix and tensor databases. In this study, 2D and 3D wind field reconstruction algorithms were developed based on POD and Tucker decomposition, respectively. Both procedures expertly and quickly obtained wind speed information for the entire area for reconstruction using extremely limited sensor measurements, which are of great significance due to their application in ultra-short-term wind prediction. A

simulation and detailed discussion were performed to validate the practicability of the algorithms. The major findings are as follows: Firstly, the reconstruction results of three boundary conditions validate that the proposed reconstruction algorithms could accurately restore the distribution characteristics of the unsteady wind field based on sparse sensors. Secondly, rearranging the matrix database into the tensor can make the data between the dimensions more closely connected, and the spatial-temporal information correlation can be obtained more effectively. Thirdly, appropriately increasing the basis vectors and 4-mode dimension reduces the reconstruction error, while excessive eigenvectors reduce the noise resistance of the system and affect the reconstruction accuracy. Fourth, in the wind field environment with prominent characteristics of wind speed distribution, the constructed database needs to contain rich speed distribution information under different boundary conditions rather than multi-time data. However, in the more complex wind field environment, diverse boundary conditions and a large number of instantaneous wind speed data are necessary. Finally, by controlling the number of sensors and improving computer performance, the reconstruction time can be reduced to the time interval of data acquisition so that data acquisition can be synchronized with wind field reconstruction, which is greatly significant in the reconstruction of the unsteady wind field.

In general, the advantage of the proposed unsteady wind field reconstruction methods is that they can greatly save calculation time (i.e., realize the synchronization of data acquisition and wind field reconstruction) while ensuring the accuracy of reconstruction, addressing the uncertainty of statistical methods and large computational loads of physical methods, which can be used in the fields of wind energy resource evaluation, wind turbine performance diagnosis and optimization of wind turbine arrangement, etc. However, it should be acknowledged that the shortcomings of the proposed algorithm are still prominent. For example, for more complex terrains and more variable entrance boundary conditions, the feasibility of the reconstruction methods needs to be verified. Moreover, in order to achieve ultra-short-term wind prediction using unsteady wind field reconstruction, there are still many studies that need to be carried out, such as experimental validation and the construction of databases using real wind field measurements. Therefore, in future research, the reliability of the reconstruction algorithms will be verified using wind tunnel experiments and real wind field data.

Author Contributions: Conceptualization, G.Z. and S.L.; methodology, G.Z. and S.L.; software, G.Z. and S.L.; validation, G.Z. and S.L.; writing—original draft preparation, G.Z.; writing—review and editing, G.Z.; project administration, S.L.; funding acquisition, S.L. All authors have read and agreed to the published version of the manuscript.

Funding: This research was supported by the National Natural Science Foundation of China grant number 61871181].

Data Availability Statement: Not applicable.

Conflicts of Interest: The authors declare no conflict of interest.

Nomenclature

Abbreviations

ANN	Artificial Neural Network
GFS	Global Forecasting System
NWP	Numerical Weather Prediction
PT	Process Tomography
CFD	Computational Fluid Dynamics
SNR	Signal-Noise Ratio
SVD	Singular Value Decomposition
PCA	Principal Component Analysis
POD	Proper Orthogonal Decomposition

Symbols	
m	Discrete sampling points in space
u	Original wind speed
$A^{(N)}$	Mode-N factorization factor matrix
$\widetilde{u}$	Measured data (m/s)
P	Measurement matrix
U	Original wind field matrix
C	Time-dependent matrix
Φ	POD mode matrix
φ_i	Basis vector
a	Modal coefficient
M	Measurement matrix
e_j	Canonical basis vector
$\mathbb{R}^n$	Real number set
RE	Relative reconstruction error
$\hat{u}$	Reconstructed wind speed
χ	Tensor
B_N	Factor matrix
$\overline{\times}_n$	n-mode tensor-vector product
$\circ$	Hadamard product
$\otimes$	Kronecker product
β_n^k	Tucker modal coefficients
ψ_n	Tucker modes
T	Tucker mode tensor
$T_{4unfold}$	Unfolding of T along the 4-mode direction
γ	Gaussian noise

References

1. Zhang, Y.; Wang, J.; Wang, X. Review on probabilistic forecasting of wind power generation. *Renew. Sustain. Energy Rev.* **2014**, *32*, 255–270. [CrossRef]
2. Okumus, I.; Dinler, A. Current status of wind energy forecasting and a hybrid method for hourly predictions. *Energy Convers. Manag.* **2016**, *123*, 362–371. [CrossRef]
3. Yan, J.; Liu, Y.; Han, S.; Wang, Y.; Feng, S. Reviews on uncertainty analysis of wind power forecasting. *Renew. Sustain. Energy Rev.* **2015**, *52*, 1322–1330. [CrossRef]
4. Erdem, E.; Shi, J. ARMA based approaches for forecasting the tuple of wind speed and direction. *Appl. Energy* **2011**, *88*, 1405–1414. [CrossRef]
5. Chen, K.; Yu, J. Short-term wind speed prediction using an unscented Kalman filter based state-space support vector regression approach. *Appl. Energy* **2014**, *113*, 690–705. [CrossRef]
6. Li, C.; Lin, S.; Xu, F.; Liu, D.; Liu, J. Short-term wind power prediction based on data mining technology and improved support vector machine method: A case study in Northwest China. *J. Clean. Prod.* **2018**, *205*, 909–922. [CrossRef]
7. Guo, Z.; Zhao, W.; Lu, H.; Wang, J. Multi-step forecasting for wind speed using a modified EMD-based artificial neural network model. *Renew. Energy* **2012**, *37*, 241–249. [CrossRef]
8. Jiang, P.; Wang, Y.; Wang, J. Short-term wind speed forecasting using a hybrid model. *Energy* **2017**, *119*, 561–577. [CrossRef]
9. Ge, M.; Wu, Y.; Liu, Y.; Li, Q. A two-dimensional model based on the expansion of physical wake boundary for wind-turbine wakes. *Appl. Energy* **2019**, *233–234*, 975–984. [CrossRef]
10. Wang, Y.; Liu, Y.; Li, L.; Infield, D.; Han, S. Short-term wind power forecasting based on clustering pre-calculated CFD method. *Energies* **2018**, *11*, 854. [CrossRef]
11. Shi, J.; Lee, W.J.; Liu, Y.; Yang, Y.; Wang, P. Forecasting power output of photovoltaic systems based on weather classification and support vector machines. *IEEE Trans. Ind. Appl.* **2012**, *48*, 1064–1069. [CrossRef]
12. Wang, H.; Yan, J.; Liu, Y.; Han, S.; Li, L.; Zhao, J. Multi-step-ahead Method for Wind Speed Prediction Correction Based on Numerical Weather Prediction and Historical Measurement Data. *J. Phys. Conf. Ser.* **2017**, *926*, 012007. [CrossRef]
13. Liu, Y.; Wang, Y.; Li, L.; Han, S.; Infield, D. Numerical weather prediction wind correction methods and its impact on computational fluid dynamics based wind power forecasting. *J. Renew. Sustain. Energy* **2016**, *8*, 033302. [CrossRef]
14. Mifsud, M.; Vendl, A.; Hansen, L.; Görtz, S. Fusing wind-tunnel measurements and CFD data using constrained gappy proper orthogonal decomposition. *Aerosp. Sci. Technol.* **2019**, *86*, 312–326. [CrossRef]
15. Khan, K.S.; Tariq, M. Wind resource assessment using SODAR and meteorological mast—A case study of Pakistan. *Renew. Sustain. Energy Rev.* **2018**, *81*, 2443–2449. [CrossRef]

16. Wang, H.; Han, S.; Liu, Y.; Yan, J.; Li, L. Sequence transfer correction algorithm for numerical weather prediction wind speed and its application in a wind power forecasting system. *Appl. Energy* **2019**, *237*, 1–10. [CrossRef]
17. Bouras, I.; Ma, L.; Ingham, D.; Pourkashanian, M. An improved k –ω turbulence model for the simulations of the wind turbine wakes in a neutral atmospheric boundary layer flow. *J. Wind Eng. Ind. Aerodyn.* **2018**, *179*, 358–368. [CrossRef]
18. Borraccino, A.; Schlipf, D.; Haizmann, F.; Wagner, R. Wind field reconstruction from nacelle-mounted lidar short-range measurements. *Wind Energy Sci.* **2017**, *2*, 269–283. [CrossRef]
19. Stathopoulos, C.; Kaperoni, A.; Galanis, G.; Kallos, G. Wind power prediction based on numerical and statistical models. *J. Wind Eng. Ind. Aerodyn.* **2013**, *112*, 25–38. [CrossRef]
20. Miyoshi, T.; Kondo, K.; Terasaki, K. Big Ensemble Data Assimilation in Numerical Weather Prediction. *Computer* **2015**, *48*, 15–21. [CrossRef]
21. Huang, X.; Wang, J.; Huang, B. Two novel hybrid linear and nonlinear models for wind speed forecasting. *Energy Convers. Manag.* **2021**, *238*, 114162. [CrossRef]
22. Marugán, A.P.; Márquez, F.P.G.; Perez, J.M.P.; Ruiz-Hernández, D. A survey of artificial neural network in wind energy systems. *Appl. Energy* **2018**, *228*, 1822–1836. [CrossRef]
23. Madhiarasan, M.; Deepa, S.N. Comparative analysis on hidden neurons estimation in multi layer perceptron neural networks for wind speed forecasting. *Artif. Intell. Rev.* **2017**, *48*, 449–471. [CrossRef]
24. Wang, H.; Lei, Z.; Zhang, X.; Zhou, B.; Peng, J. A review of deep learning for renewable energy forecasting. *Energy Convers. Manag.* **2019**, *198*, 111799. [CrossRef]
25. Zhang, J.; Draxl, C.; Hopson, T.; Monache, L.D.; Vanvyve, E.; Hodge, B.M. Comparison of numerical weather prediction based deterministic and probabilistic wind resource assessment methods. *Appl. Energy* **2015**, *156*, 528–541. [CrossRef]
26. Jung, J.; Broadwater, R.P. Current status and future advances for wind speed and power forecasting. *Renew. Sustain. Energy Rev.* **2014**, *31*, 762–777. [CrossRef]
27. Candy, B.; English, S.J.; Keogh, S.J. A comparison of the impact of QuikScat and winds at wind vector products on met office analyses and forecasts. *IEEE Trans. Geosci. Remote Sens.* **2009**, *47*, 1632–1640. [CrossRef]
28. Watson, S.J.; Landberg, L.; Halliday, J.A. Application of wind speed forecasting to the integration of wind energy into a large scale power system. *IEE Proc. Gener. Transm. Distrib.* **1994**, *141*, 357–362. [CrossRef]
29. Prakoso, A.T.; Basri, H.; Adanta, D.; Yani, I.; Ammarullah, M.I.; Akbar, I.; Ghazali, F.A.; Syahrom, A.; Kamarul, T. The Effect of Tortuosity on Permeability of Porous Scaffold. *Biomedicines* **2023**, *11*, 427. [CrossRef]
30. Putra, R.U.; Basri, H.; Prakoso, A.T.; Chandra, H.; Ammarullah, M.I.; Akbar, I.; Syahrom, A.; Kamarul, T. Level of Activity Changes Increases the Fatigue Life of the Porous Magnesium Scaffold, as Observed in Dynamic Immersion Tests, over Time. *Sustainability* **2023**, *15*, 823. [CrossRef]
31. Reja, R.K.; Amin, R.; Tasneem, Z.; Ali, M.F.; Islam, M.R.; Saha, D.K.; Badal, F.R.; Ahamed, M.H.; Moyeen, S.I.; Das, S.K. A review of the evaluation of urban wind resources: Challenges and perspectives. *Energy Build.* **2022**, *257*, 111781. [CrossRef]
32. Sun, S.; Liu, S.; Zhang, G. The Rapid Establishment of Large Wind Fields via an Inverse Process. *Appl. Sci.* **2019**, *9*, 2847. [CrossRef]
33. Jiang, C.; Soh, Y.C.; Li, H. Sensor and CFD data fusion for airflow field estimation. *Appl. Therm. Eng.* **2016**, *92*, 149–161. [CrossRef]
34. Qin, L.; Liu, S.; Long, T.; Shahzad, M.A.; Schlaberg, H.I.; Yan, S.A. Wind field reconstruction using dimension-reduction of CFD data with experimental validation. *Energy* **2018**, *151*, 272–288. [CrossRef]
35. Zhang, G.; Zheng, X.; Liu, S.; Chen, M. Three-dimensional wind field reconstruction using tucker decomposition with optimal sensor placement. *Energy* **2022**, *260*, 125098. [CrossRef]
36. Astrid, P.; Weiland, S.; Willcox, K.; Backx, T. Missing point estimation in models described by proper orthogonal decomposition. *IEEE Trans. Automat. Contr.* **2008**, *53*, 2237–2251. [CrossRef]
37. Noack, B.R. Turbulence, Coherent Structures, Dynamical Systems and Symmetry. *AIAA J.* **2013**, *51*, 2991. [CrossRef]
38. Sirovich, L. Turbulence and the dynamics of coherent structures. Part I: Coherent structures. Part II: Symmetries and transformations. Part III: Dynamics and scaling. *Q. Appl. Math.* **1987**, *45*, 561–590. [CrossRef]
39. Veganzones, M.A.; Cohen, J.E.; Farias, R.C.; Chanussot, J.; Comon, P. Nonnegative Tensor CP Decomposition of Hyperspectral Data. *IEEE Trans. Geosci. Remote Sens.* **2016**, *54*, 2577–2588. [CrossRef]
40. Kolda, T.G.; Bader, B.W. Tensor decompositions and applications. *SIAM Rev.* **2009**, *51*, 455–500. [CrossRef]
41. Luo, X.; Zhang, Z.; Zhang, C.; Wu, X. Multi-focus image fusion using HOSVD and edge intensity. *J. Vis. Commun. Image Represent.* **2017**, *45*, 46–61. [CrossRef]
42. Chao, T.T.; Sanzolone, R.F. Decomposition techniques. *J. Geochemical Explor.* **1992**, *44*, 65–106. [CrossRef]
43. Luh, G.; Lin, C. PCA based immune networks for human face recognition. *Appl. Soft Comput. J.* **2011**, *11*, 1743–1752. [CrossRef]
44. Hieu, T.; Maday, Y.; Guillo, M.; Guérin, P. A new method for reconstruction of cross-sections using Tucker decomposition. *J. Comput. Phys.* **2017**, *345*, 189–206. [CrossRef]
45. Tauviqirrahman, M.; Jamari, J.; Susilowati, S.; Pujiastuti, C.; Setiyana, B.; Pasaribu, A.H.; Ammarullah, M.I. Performance Comparison of Newtonian and Non-Newtonian Fluid on a Heterogeneous Slip/No-Slip Journal Bearing System Based on CFD-FSI Method. *Fluids* **2022**, *7*, 225. [CrossRef]
46. Ammarullah, M.I.; Hartono, R.; Supriyono, T.; Santoso, G.; Sugiharto, S.; Permana, M.S. Polycrystalline Diamond as a Potential Material for the Hard-on-Hard Bearing of Total Hip Prosthesis: Von Mises Stress Analysis. *Biomedicines* **2023**, *11*, 951. [CrossRef] [PubMed]

47. Ammarullah, M.I.; Santoso, G.; Sugiharto, S.; Supriyono, T.; Wibowo, D.B.; Kurdi, O.; Tauviqirrahman, M.; Jamari, J. Minimizing Risk of Failure from Ceramic-on-Ceramic Total Hip Prosthesis by Selecting Ceramic Materials Based on Tresca Stress. *Sustainability* **2022**, *14*, 13413. [CrossRef]
48. Tauviqirrahman, M.; Ammarullah, M.I.; Jamari, J.; Saputra, E.; Winarni, T.I.; Kurniawan, F.D.; Shiddiq, S.A.; van der Heide, E. Analysis of contact pressure in a 3D model of dual-mobility hip joint prosthesis under a gait cycle. *Sci. Rep.* **2023**, *13*, 3564. [CrossRef]
49. Ammarullah, M.I.; Afif, I.Y.; Maula, M.I.; Winarni, T.I.; Tauviqirrahman, M.; Akbar, I.; Basri, H.; van der Heide, E.; Jamari, J. Tresca stress simulation of metal-on-metal total hip arthroplasty during normal walking activity. *Materials* **2021**, *14*, 7554. [CrossRef] [PubMed]
50. Jamari, J.; Ammarullah, M.I.; Santoso, G.; Sugiharto, S.; Supriyono, T.; Permana, M.S.; Winarni, T.I.; van der Heide, E. Adopted walking condition for computational simulation approach on bearing of hip joint prosthesis: Review over the past 30 years. *Heliyon* **2022**, *8*, e12050. [CrossRef] [PubMed]
51. Jamari, J.; Ammarullah, M.I.; Santoso, G.; Sugiharto, S.; Supriyono, T.; van der Heide, E. In Silico Contact Pressure of Metal-on-Metal Total Hip Implant with Different Materials Subjected to Gait Loading. *Metals* **2022**, *12*, 1241. [CrossRef]
52. Salaha, Z.F.M.; Ammarullah, M.I.; Abdullah, N.N.A.A.; Aziz, A.U.A.; Gan, H.; Abdullah, A.H.; Abdul Kadir, M.R.; Ramlee, M.H. Biomechanical Effects of the Porous Structure of Gyroid and Voronoi Hip Implants: A Finite Element Analysis Using an Experimentally Validated Model. *Materials* **2023**, *16*, 3298. [CrossRef]
53. Jamari, J.; Ammarullah, M.I.; Saad, A.P.M.; Syahrom, A.; Uddin, M.; van der Heide, E.; Basri, H. The effect of bottom profile dimples on the femoral head on wear in metal-on-metal total hip arthroplasty. *J. Funct. Biomater.* **2021**, *12*, 38. [CrossRef]
54. Jamari, J.; Ammarullah, M.I.; Santoso, G.; Sugiharto, S.; Supriyono, T.; Prakoso, A.T.; Basri, H.; van der Heide, E. Computational Contact Pressure Prediction of CoCrMo, SS 316L and Ti6Al4V Femoral Head against UHMWPE Acetabular Cup under Gait Cycle. *J. Funct. Biomater.* **2022**, *13*, 64. [CrossRef]
55. Allab, K.; Labiod, L.; Nadif, M. A Semi-NMF-PCA Unified Framework for Data Clustering. *IEEE Trans. Knowl. Data Eng.* **2017**, *29*, 2–16. [CrossRef]
56. Moreno, A.I.; Jarzabek, A.A.; Perales, J.M.; Vega, J.M. Aerodynamic database reconstruction via gappy high order singular value decomposition. *Aerosp. Sci. Technol.* **2016**, *52*, 115–128. [CrossRef]